

## Effect of mechanical error on dual-wedge laser scanning system and error correction

YUNHAO GE,<sup>1</sup> JIHAO LIU,<sup>1</sup> FENFEN XUE,<sup>2</sup> ENGUANG GUAN,<sup>1</sup> WEIXIN YAN,<sup>1</sup> AND YANZHENG ZHAO<sup>1,\*</sup>

<sup>1</sup>State Key Lab of Mechanical System and Vibration, School of Mechanical Engineering, Shanghai Jiao Tong University, Shanghai 200240, China

<sup>2</sup>Shanghai Aerospace Control Technology Institute, Shanghai 200240, China

\*Corresponding author: yzh-zhao@sjtu.edu.cn

Received 23 February 2018; revised 7 June 2018; accepted 17 June 2018; posted 18 June 2018 (Doc. ID 318730); published 17 July 2018

Compared with the traditional mechanical beam deflector in a beam-scanning system, the dual-wedge scanning system has several advantages, for example, compact structure, fast scanning speed, and low power consumption. High accuracy is the most important factor in dual-wedge scanning, but mechanical errors caused by machining or assembly errors adversely affect this scanning accuracy. Horizontal and angular mechanical errors appear between the incident light and the dual-wedge central optical axes. By building a mathematical model of an ideal dual-wedge scanning trajectory and a trajectory affected by mechanical errors, this paper analyzes the types and degree of influence on the scanning process, as well as the sensitivity of scanned images to different errors. Results show that the angular error has the most significant influence on the scanning image accuracy, in terms of trajectory shape and coverage. To correct the angular error, the two degrees-of-freedom flexible fine-tuning mechanism is customized based on the principle of the cantilever beam type. After finite element analysis and experimental validations, the fine-tuning mechanism can guarantee that the angular error in the dual-wedge central optical axes will be lower than 0.05 deg, thus ensuring scanning trajectory accuracy. © 2018 Optical Society of America

**OCIS codes:** (140.3490) Lasers, distributed-feedback; (060.2420) Fibers, polarization-maintaining; (060.3735) Fiber Bragg gratings.

<https://doi.org/10.1364/AO.57.006047>

### 1. INTRODUCTION

As a popular beam deflector in the beam-scanning system, the dual-wedge scanning system is widely used in image motion compensation [1], target tracking [2], pulsed polarization/depolarization [3], and high-precision angular generation [4–6]. Compared to a traditional beam-scanning system based on mechanical deflection, dual-wedge scanning is outstanding in enlarging the field of view and search range in addition to its advantages of a compact structure, fast scanning speed, and low power consumption. In terms of design, Li [7,8], Wei [9], and Li [10] carried out a theoretical derivation analysis of the dual-wedge optical path scanning trajectory. Xiao [11], Lei [6], and Li [12] designed a dual-wedge scanning mechanism for use with imaging guidance and scanning. Marshall [13] placed Risley prism scanners in the general context of optical scanners and researched the crucial rules in application of Risley prism scanners.

High resolution and accuracy play significant roles in the dual-wedge scanning system. Marshall [14] presented a set of generated scan patterns that include regular polygons by selecting particular values for the ratios of angular speeds. And Duma proposed a novel graphical method to complete the exact modeling of the scanning process, which enables

to choose the most appropriate parameters of the device and enlarge the specific application [15]. As for all laser scanners, internal factors (e.g., steady rotation speed of the motor and double-wedge manufacturing technology) have been improved to improve these features in previous works. Li analyzed the beam distortion theory of dual-wedge scanning under arbitrary incident angles and found that the wedge angles and refractive indices of the prisms greatly influenced beam distortion [16]. However, the mechanical error analysis and application of error correction are rare: external factors, including manufacturing and assembly errors, can lead to deviation in the optical wedge center axes, affecting the resolution and accuracy of the dual-wedge scanning trajectory.

The dual-wedge laser scanning system is composed of optical wedges, bearings, power components, transmission components, and other mechanisms. Errors occurring during the manufacturing and assembly process will lead to deviations between the actual and ideal positions of the optical wedge. Deviation, including horizontal and angular kinds, between the dual-wedge optical central axis and the laser incident ray path, may change the light deflection angle and exit direction. This can cause deformation, displacement, and serious coverage vacancy in the scanned trajectory. Thus, studying the effects of

mechanical errors and correction can significantly improve accuracy and resolution.

This paper explores approaches and degrees of influence on the scanning process due to different errors, as well as the sensitivity of scanned images to different errors. By establishing a mathematical model of dual-wedge scanning, a trajectory equation of image scanning under the influence of each deviation can be analyzed theoretically. The proposed analysis compares the impacts of different deviations on a scanned image. Then, a targeted correction method is developed based on a flexible mechanism, which relies on its own deformation to achieve smooth displacement and force. The entire process, without friction, wear, or transmission gaps, can achieve high-precision movement [17]. In this paper, a two degrees-of-freedom (DOF) fine-tuning mechanism based on a cantilever beam is proposed and explored [18], which guarantees that the angular deviation of the center optical axis of the double wedge will be below 0.05 deg. Finally, the feasibility and effectiveness of the scanning system are verified by finite element analysis and practical experiments.

## 2. DUAL-WEDGE REFRACTION AND IDEAL SCANNING TRAJECTORY

By using the Fresnel refraction and reflection law to study the optical path, results show that the wedge will always deflect the direction of the incident ray to the side with the greatest increasing slope of wedge thickness. The distance between the double wedges and wedge thickness have no effect on beam deflection [16]. Marshall's characteristic parameters are utilized [14]: ( $A$ ) represents the fixed refracting angle, ( $D$ ) represents the beam's vectorial angular deviations of the prism. The deflection angle ( $D$ ) and refractivity ( $n$ ) approximate the formula 1:

$$D = (n - 1)A. \quad (1)$$

Let  $\omega_1$  and  $\omega_2$  represent the beam's rotation speeds of prism 1 and prism 2, respectively.  $\varphi_{01}$  and  $\varphi_{02}$  represent the initial phase of the two prisms, respectively. In this paper, we use two same prisms in the application of the dual-wedge laser scanning system. Thus, the ratio of the beam deviations  $k$  is 1, while the ratio between the rotation speed of prism 2 and prism 1 ( $\omega_2/\omega_1$ ) is variable parameter  $M$ . As shown in Fig. 1(a), which is one of the configurations of a dual-wedge where two wedges are back to back in parallel, the total diagonal angle of the dual wedges is within the range of  $0-2D$ . Figure 1(b) shows an equivalent model when  $M < 0$ . The total deflection angle  $\Theta$  can be obtained by any real-time phases ( $\varphi_1$  and  $\varphi_2$ , respectively) of the two vectors;  $t$  represents arbitrary instants:

$$\Theta = 2D \cos\left(\frac{(\omega_1 t + \varphi_{01}) + (\omega_2 t + \varphi_{02})}{2}\right). \quad (2)$$

To specify physical meaning, a standard equation that expresses the double-wedge scanned image is as follows [14]:

$$\begin{cases} D_x = D[\cos(\omega_1 + \varphi_{01}) + \cos(\omega_2 + \varphi_{02})] \\ D_y = D[\sin(\omega_1 + \varphi_{01}) + \sin(\omega_2 + \varphi_{02})] \end{cases} \quad (3)$$

where  $\omega_1$  and  $\omega_2$  are in opposite directions. The scanned image resembles rose petals [19], a natural and useful scanning method in target tracking. In Fig. 1(c),  $R$  is the petal length

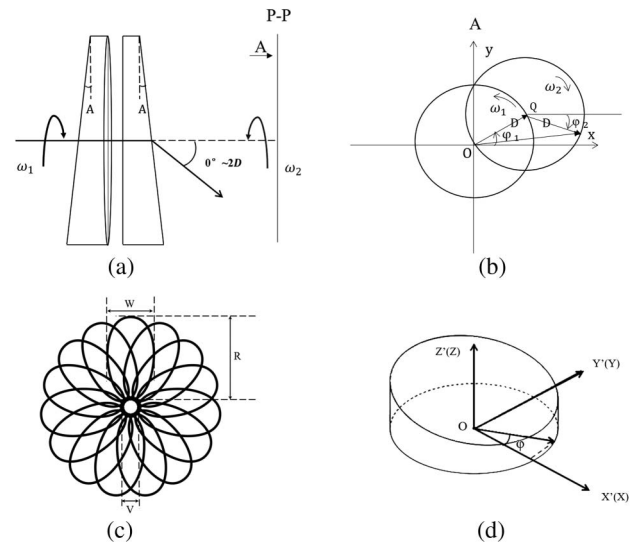


**Fig. 1.** (a) One of the configurations of dual-wedge; (b) rotating double-wedge equivalent vector model when the  $M < 0$ ; (c) rose petals scanned image when  $M < 0$ ; (d) initial state of two coordinate systems.

of the scanned image, namely the field radius;  $W$  refers to the petal width;  $V$  is the diameter of the central vacancy; and  $N$  is the number of rose petals. Figure 1(d) shows two systems of coordinates. The first (the world coordinate system) is based on the horizontal plane as the base  $X-O-Y$ , vertically perpendicular to the ground as the  $Z$  axis; the second (the local coordinate system) is a Cartesian coordinate system built on the wedge. The maximum and minimum values of the wedge heights are in the plane  $X'-O-Z'$ . In the initial state (when the optical wedge is standard installed), the two coordinate systems coincide.

## 3. EFFECTS OF DIFFERENT ERRORS ON THE SCANNING TRAJECTORY

Figure 2 shows three main causes of mechanical errors in dual-wedge scanning: (a) a horizontal error  $d$  between the incident ray and the central optical axis; (b) a horizontal error  $d_1$  between the two optical axes of the double wedge; and (c) an angular error  $\beta$  between the incident ray and the central axis of the optical wedge.

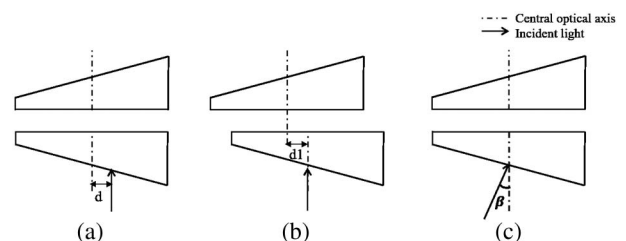


**Fig. 2.** Schematics of three main deviations caused by mechanical errors.

### A. Horizontal Error between the Incident Ray and Central Optical Axis

Figure 3 shows the trajectory details, where  $\Delta d$  denotes the difference between the ideal and actual ray path passing through the first wedge. The projected deflection distances  $L$  and  $L'$  caused by optical path deviation are different. As the optical wedge rotates at an angular velocity  $\omega$ , the distance deviation  $\Delta d$  changes, resulting in a fluctuation of the deflection distance  $L'$ , which causes an error in the scanned trajectory.

Using equivalent methodology, it is assumed that the optical wedge does not rotate. The incident ray rotates around the central optical axis at an angular velocity  $\omega$  with the same distance  $d$ .

In the wedge local coordinate system  $O-XYZ$ , the optical path difference is obtained as a function of the error  $d$  and the optical wedge phase  $\varphi$ :

$$\Delta d = d \cos(\varphi) \tan(A). \quad (4)$$

Under this error, when the ray passes through a single wedge, the ray-scanned trajectory is rewritten as

$$\begin{cases} x = l' \cos(\varphi) = [P + d \cos(\omega t) \tan(A)] \tan(\delta) \cos(\omega t) \\ y = l' \sin(\varphi) = [P + d \cos(\omega t) \tan(A)] \tan(\delta) \sin(\omega t) \end{cases} \quad (5)$$

where  $P$  is the vertical distance from incident point to projection plan, and  $l$  and  $l'$  are scanning distances. Next, the scanning trajectory is investigated when the ray enters the double optical wedges. As shown in Fig. 3, when the ray reaches the second wedge, horizontal errors between the incident ray and the standard ray are denoted as  $d'$ , while the path difference changes to  $\Delta d'$ :

$$d' = \frac{d \cos(A - D)}{\cos(A) \cos(D)}, \quad (6)$$

$$\Delta d' = d' \cos(\theta) \tan(A). \quad (7)$$

The horizontal error only affects the length of the optical path and has no effect on light deflection angles; therefore, the trajectory equation of the scanned image of double optical wedges under the influence of deviations can be obtained thusly:

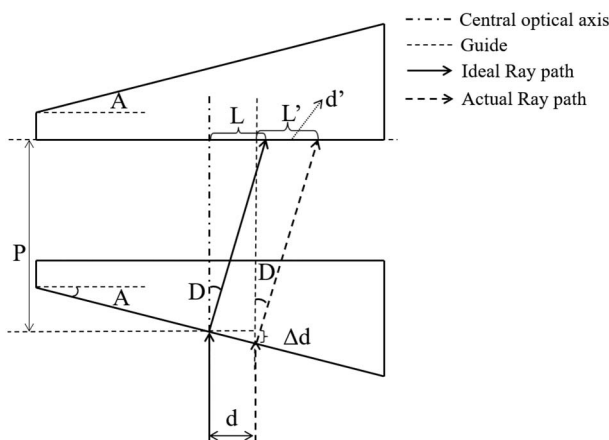


**Fig. 3.** Schematics of the horizontal error between the incident ray and central optical axis and the approximate trajectory.

**Table 1.** Initial Parameters of the Scanning Trajectory

Parameter Name	Symbol	Value
Refractive edges (wedge angle)	$A$	4 deg
Refractive index (material)	$n$	Ordinary glass/1.5
Deflection angle	$D$	2 deg
Motor speed ratio	$M$	-5:8
Initial phase	$\varphi_0 1: \varphi_0 2$	$\pi$
Scanning distance	$P$	1000 mm

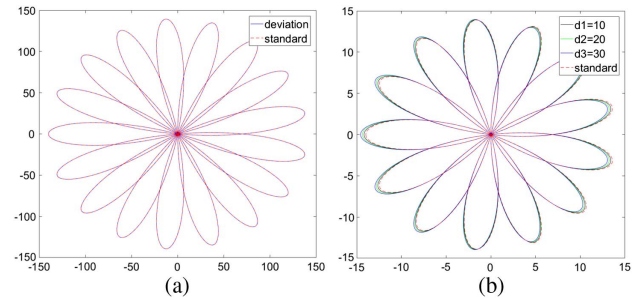


**Fig. 4.** Scanned image with horizontal error.

$$\begin{cases} x'(t) = \frac{[1 + d \cos(\varphi) \tan(A) + \frac{d \cos(A+D) \cos(\varphi) \tan(A)}{\cos(A) \cos(D)}] \tan(2D)}{2} \\ y'(t) = \frac{[\cos(\omega_1 + \varphi_0 1) + \cos(\omega_2 + \varphi_0 2)] [1 + d \cos(\varphi) \tan(A) + \frac{d \cos(A+D) \cos(\varphi) \tan(A)}{\cos(A) \cos(D)}] \tan(2D)}{2 [\sin(\omega_1 + \varphi_0 1) + \sin(\omega_2 + \varphi_0 2)]} \end{cases} \quad (8)$$

According to the scanning trajectory, the initial parameters are shown in Table 1.

The standard rose-shaped scanned image can be obtained from Eq. (3), indicated by the dotted sections in Fig. 4; all units are measured in millimeters. From Eq. (8), the scanned image of the double wedge under the influence of the horizontal error is the solid line in Fig. 4(a). In the image, the horizontal incident error has a minor effect of nearly 0.05 mm. To qualitatively analyze the effect of horizontal errors on the scanned image, the scanning distance  $l$  is shortened, and the horizontal error  $d$  is increased by gradients. The curve of the rose line under different errors (mm) is shown in Fig. 4(b).

The horizontal error and scanning distance are not an order of magnitude, where the scanning distance is much larger than the horizontal error. The horizontal error  $d$  has little effect on the length  $R$  and width  $W$  of the scanned image petals; it also has no influence on the number of rose petals  $N$ . However, the present analysis indicates that horizontal error affects the shape and end position of the petal; that is, the petal shape of the envelope is roughly in the shape of an apple instead of a rounded circle.

### B. Horizontal Error between the Center Optical Axes of the Double Wedge

When the double wedge shows a horizontal error  $d_1$  between the double central axes, the scanning image trajectory equation led by horizontal error  $d_1$  can be obtained:

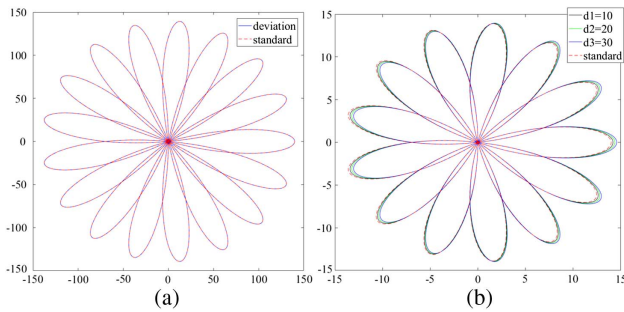


**Fig. 5.** Dual-wedge scanning image with horizontal error between the center optical axes.

$$\begin{cases} x'(t) = \frac{[1 + d_1 \cos(\varphi) \tan(A)] \tan(2D)}{2} \\ y'(t) = \frac{[\cos(\omega_1 + \varphi_0 1) + \cos(\omega_2 + \varphi_0 2)]}{2} \end{cases} \quad (9)$$

The scanned image in Fig. 5(a) demonstrates that the effect of the horizontal error  $d_1$  can be neglected. Figure 5(b) presents a detailed qualitative analysis of the error  $d_1$  where the distance  $l$  is shortened, and the horizontal error  $d_1$  is increased by equal ratio gradients. The error slightly affects the shape and end position of the petal, similar to that caused by the horizontal error  $d$  of the incident ray and central optical axis.

### C. Angular Error between the Incident Ray and Center Optical Axis

When the angle error  $\beta$  appears between the incident ray and central optical axis, any deflection of the optical wedge can be divided into the rotations around the  $X$  and  $Y$  axes, respectively. The angles of projection of the outgoing ray in the  $Y-O-Z$  plane and the  $X-O-Z$  plane are explored individually.

When the angle error  $\beta$  is presented as the rotation around the  $Y$  axis, the projection of the optical wedge on the  $Y-O-Z$  plane is in the shape of a rectangle, and the outgoing ray does not produce an angular error. Figure 6 illustrates the projection of the optical wedge on the  $X-O-Z$  surface

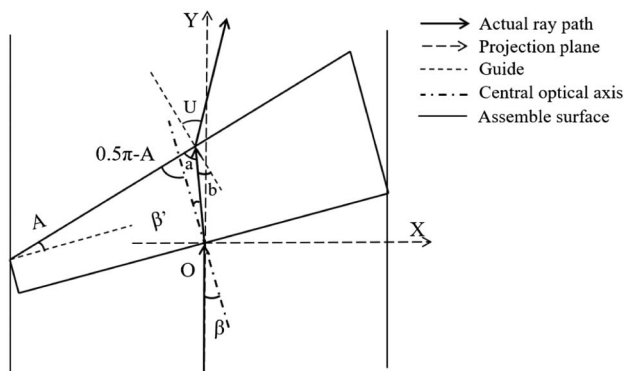


**Fig. 6.** Projection in  $X-O-Z$  under the angle error  $\beta$  presented as rotation around the  $Y$  axis.

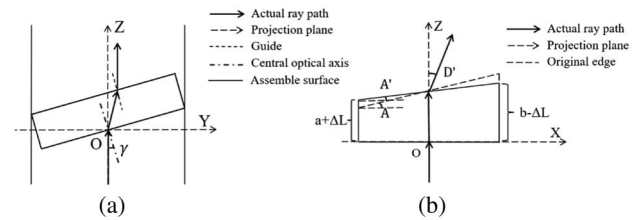


**Fig. 7.** (a) Projection in  $Y-O-Z$  plane; (b) projection in  $X-O-Z$  plane under angle error  $\gamma$  expressed as rotation around the  $X$  axis.

under the same error. According to Fresnel's law and the optical refraction reflection law, where  $a$ ,  $b$ , and  $\beta'$  are the intermediate angular variables, the deviation angle of the outgoing ray coincides with the ideal angle without error. The wedge angle error  $\beta$  can be presented as the rotation angle around the  $Y$  axis.

When the wedge angle error  $\gamma$  is expressed as rotation around the  $X$  axis, the projection on the  $Y-O-Z$  surface appears, as shown in Fig. 7(a). The angle of the outgoing ray does not change. Figure 7(b) depicts the projection on the  $X-O-Z$  plane, indicating that the longest side of the optical wedge  $b$  is reduced by  $\Delta L$  with an increase in the error angle  $\gamma$ ; rather, the shortest edge  $a$  increases by  $\Delta L$ . This circumstance can be equivalent to a reduced optical wedge angle from  $\alpha$  to  $\alpha'$ , wherein the deflection angle decreases to  $\delta'$ , thus affecting the scanned trajectory. The angular deviation is expressed as a superimposition between a rotation around the  $X$  and  $Y$  axes. As long as the deviation around the  $X$  axis rotation occurs, the final exit angle changes with respect to the standard case, and the angular deviation direction is different under different errors. The two wedges are seen as two rotating vectors  $Z_1$  and  $Z_2$  when rotating at a certain speed, as shown in Fig. 8. The angular deflection of the incident ray becomes  $\Phi'$ , and the size and direction of the incident angle error  $\beta$  are influenced by the process of assemble, which can be treated as random in statistics and probability. As a result, the ray deflection of the double wedge consists of random variables within a certain range of error. According to the parallelogram method of vector superposition, the scanning image trajectory equation of the rose line can be obtained:

$$\theta'^2 = (z_1 \sin \varphi_1 - z_2 \sin \varphi_2)^2 + (z_1 \cos \varphi_1 - z_2 \cos \varphi_2)^2, \quad (10)$$

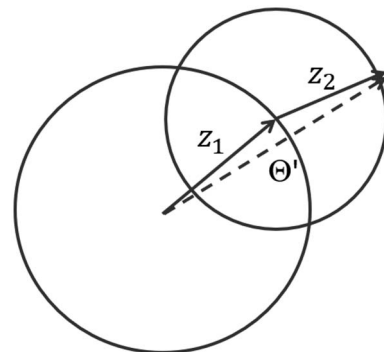


**Fig. 8.** Equivalent schematic for the angle deviation vector.



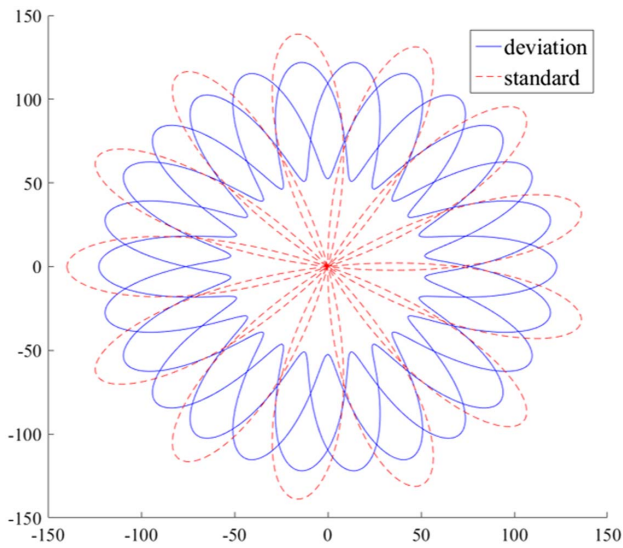


Fig. 9. Dual-wedge scanning image with angle error.

$$\begin{cases} x = \varphi' \cos(\varphi) \\ y = \varphi' \sin(\varphi) \end{cases} \quad (11)$$

Under the influence of the angle error, the angular deviation of light increased by 3 deg after passing through the incident wedge, and the angle deviation of light declined by 1.5 deg after passing through the exit wedge.

Figure 9 shows that a serious vacancy appears in the center of the scanned image; the size of the vacancy is determined by the ratio of deflection angles  $z_1$  and  $z_2$ , which are caused by the angle error. The number of rose petals doubles, and the petal length is significantly shorter while the width is invariable but heavily overlapped. The angular error poses significant influence on the scanning range and scanning precision. After adjusting the speed ratio  $M$  to 1:-1 [14], the scanning simulation can be obtained under reverse constant speed rotation. The axis range, shown in Fig. 10, coincides with a short scanning range of the ordinate because the axes measurement unit is in

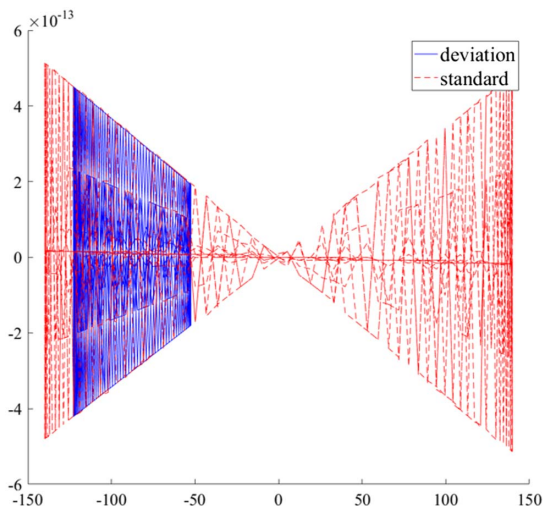


Fig. 10. Dual-wedge scanning image with angle error under isokinetic reverse scanning.

Table 2. Characteristics of the Influences of the Three Errors

Error Types	Influence Items on Scan Trajectory	Influence Degree
Horizontal error $d$ between the incident ray and the central optical axis	Petal length ( $R$ ), envelope curve shape	Minor impact, can be neglected in application
Horizontal error $d_1$ between the two optical axes of the double wedge	Petal length ( $R$ ), envelope curve shape	Minor impact, can be neglected in application
Angular error $\beta$ between the incident ray and the central axis of the optical wedge	Petal length ( $R$ ), envelope curve shape, scan area, petal width $W$ , diameter of the central vacancy $V$	Main impact, severely damage performance

millimeters; thus, the standard trajectory is equal to a straight line swinging around the center point. On the contrary, the angle error limits the scanned range on only one side of the center.

Three errors are included in the simulation; the resultant image was basically the same as that displayed in Fig. 10. Thus, our conclusions are as follows: (1) Because the dual-wedge scanning distance is much larger than the size of the horizontal error caused by the parallel axis deviation, the influence of the horizontal error is so small that it can be ignored. (2) The angle error leads to major effects of three mechanical errors on the scanning images. The shape, position, and petal number of the scanned image changed greatly, exerting significant influence on the scanning range and scanning precision. To sum up, we use Table 2 to summarize the characteristics of the influences of the three errors.

#### 4. STUDY OF ERROR CORRECTION BASED ON THE FINE-TUNING MECHANISM

##### A. Principle of Fine-Tuning Mechanism Based on the Cantilever Beam

With a small degree of elastic deformation, as shown in Fig. 11, the cantilever beam can achieve quantitative bending. When the optical wedge is mounted on the cantilever beam, the angle of the central axis of the optical wedge deflects with the cantilever beam's deformation; thus, angular deviation of the dual-wedge optical axis caused by errors in machining accuracy or assembly is eliminated.

The adjustment angle of the wedge optical axis ranges from  $-1$  deg to  $1$  deg. First, the maximum deflection required to adjust the deflection angle range can be obtained according to deflection Eq. (12) and corner Eq. (13) of the cantilever beam [20,21]:

$$y = -\frac{Px^2}{6EI}(3l - x), \quad (12)$$

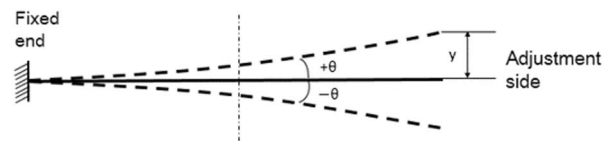


Fig. 11. Schematic for flexible cantilever beam.

$$y = -\frac{PI^2}{2EI}, \quad (13)$$

where  $E$  is the modulus of elasticity;  $I$  is the cross-section inertia;  $x$  is the distance from the fixed end to the adjustment screw;  $l$  is the cantilever length;  $y$  is the maximum deflection; and  $\Theta$  is the corner.

## B. Scanning Fine-Tuning Mechanism Design and Verification

The fine-tuning mechanism is used as the core structure to eliminate the optical axis deflection in the wedge center, which is mainly composed of the flexible cantilever beam, adjusting screw, and connecting parts. As shown in Fig. 12, to prevent adjusted deformation from affecting the drive motor assembly, we slotted in the middle of the optical wedge-bearing installation area and the motor assembly area. The screw was chosen as the adjustment part, and the double upper screws and double down screws were set. Each wedge achieved a two-degrees-of-freedom error correction for the fine-tuning mechanism rotating around the  $Z$  and  $X$  axes. Adjustment results are shown in Table 3. A finite element simulation, force analysis, and verification under ultimate strength were carried out. The flexible cantilever material was made of aluminum alloy (grade 7075 with corrosion resistance, high oxidation resistance, and good processing). The length was approximately 110 mm with a width of 50 mm and thickness of 10 mm. In the simulation, the optical axes in the four directions were adjusted through cooperation of the screw and the laminating mechanism. The adjustment was carried out to the ultimate position, as shown in Fig. 13. The gap structure of the coordination structure was designed according to the maximum deflection, and the adjusted screws were designed according to the force from Eq. (14) under maximum strain conditions [21]:

$$d_1 \geq \sqrt{\frac{F_c}{\frac{\pi}{4}[\sigma]}} = \sqrt{\frac{F_c}{\frac{\pi}{4}\sigma_s}}. \quad (14)$$

In this formula,  $F_c$  is the axial load (N);  $d_1$  is the bolt trails (mm);  $\sigma_s$  is the yield strength (MPa), determined by the mechanical

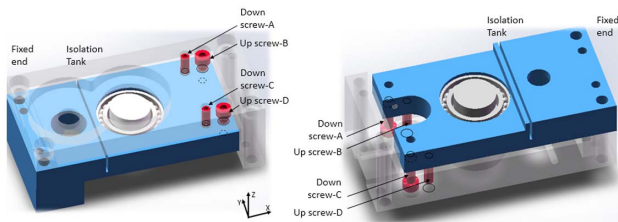


**Fig. 12.** Fine-tuning mechanism model based on the flexible cantilever beam.

grade of the thread connection and the material of the connected parts;  $[\sigma]$  is permissible stress (MPa); and  $S_s$  is the axial load safety factor.

Finally, the  $M4$  adjustment screw was chosen to adjust the fine-tuning mechanism, and the countersunk head screw was selected in the upward adjustment process. The rotating dual-wedge system projects the collimated laser beam onto the wedge pair that rotates around the same axis, so the outgoing ray is emitted at a predetermined angle and direction. Due to optical wedge assembly and axis adjustments requirements, the overall equipment was installed as a cascade combination. The three-dimensional model and section view of the dual-wedge laser scanning mechanism based on the flexible fine-tuning mechanism appear in Fig. 14.

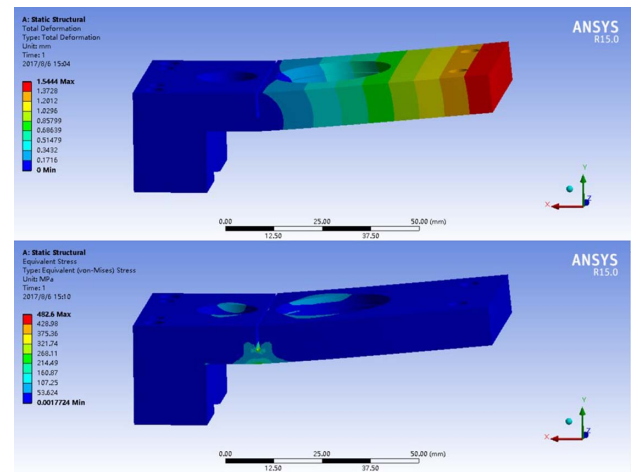


**Fig. 13.** Finite element simulation of the wedge in an ultimate position.

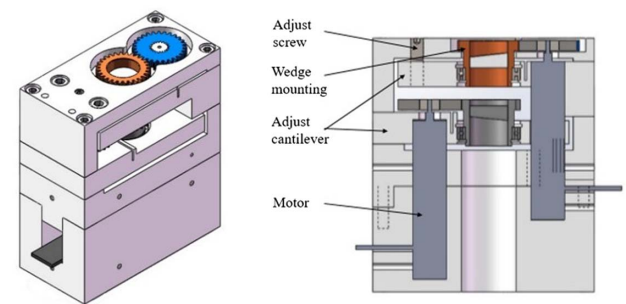


**Fig. 14.** Full view and section view of the laser-scanning mechanism based on the optical wedge.

**Table 3.** Adjustment Range and Force Analysis of the Fine-Tuning Mechanism

Direction Adjustment	Upper Wedge Adjustment Screw	Lower Wedge Adjustment Screw	Maximum Deformation (mm)	Ultimate Stress (Mpa)	Ultimate Adjustment Angle (deg)
Rotate clockwise around the $Z$ axis	$A, C$	$B, D$	1.5	480	1.3
Rotate clockwise around the $Z$ axis	$B, D$	$A, C$	1.5	480	-1.3
Rotate clockwise around the $X$ axis	$A, D$	$A, D$	0.45	350	0.5
Rotate clockwise around the $X$ axis	$B, C$	$B, C$	0.45	350	-0.5

## 5. EXPERIMENTAL VALIDATION RESULTS AND DISCUSSION

Performance experiments were used to verify the adjustment effect of the fine-tuning mechanism on the dual-wedge scanning process. The required equipments for the experimental platform are as follows.

As shown in Fig. 15, the laser emission mechanism emits the ray source required by the test after collimation. The brushless DC servo motor driver controls the speed of two high-speed brushless DC servo motors in real time. A semi-closed-loop control is used in motor control. The clamping and fixing mechanisms set the required height of the fine-tuning mechanism and the light plate. The display board shows the laser scanning location and the experimental results. Due to laser collimation, the scanning spot particles are relatively large, and the track resolution is low. To avoid laser damage and for the safety of the experimenter, the distance between the laser-emitting mechanism and the light-emitting panel was controlled. First, an experiment involving the dual-wedge fine-tuned mechanism under same-speed rotation in the same direction was carried out. Figure 16 shows the scan results at high and low speeds, respectively, after fine machine trimming.

The high-speed scanning results demonstrated precise circles, whereas the low-speed scan produced incomplete circles because under the high inertia load, the motor has fluctuation of speed at the range of 400 to 800 rpm. The circle scan shape is matched with the ideal theoretical result of the corrected system, where the double wedge with same-speed rotation was equal to a single wedge with a magnified deflection angle. Then, an experiment involving a dual-wedge fine-tuned mechanism under reverse isokinetic rotation was carried out. The double wedge speed ratio was 1:-1. Scan results are shown in Fig. 17. The scanned image was symmetrical around the origin. Although accuracy was limited, the image can be seen clearly; the dots are symmetrical and pass through the origin. Theoretically, if the mechanical angular error was not corrected, the scanned image would be a straight line within the unilateral limit region and could not pass through the origin. The experimental result indicates that the fine-tuning mechanism

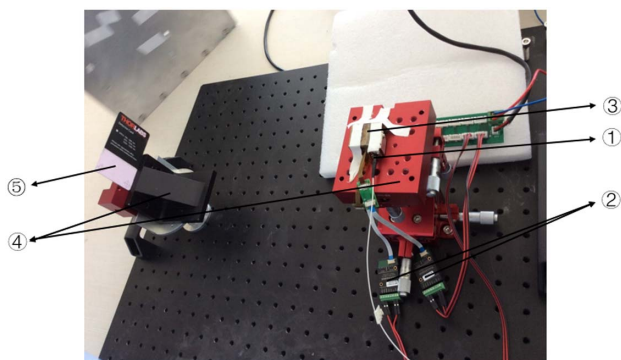


**Fig. 15.** Dual-wedge scanning mechanism experiment platform: (1) laser emission mechanism, (2) brushless DC servo motor driver (MCBL 3002), (3) dual-wedge laser scanning mechanism with brushless DC servo motor (Faulhaber 0515B) and fine-tuning mechanism, (4) clamping and fixing mechanism, (5) display board.

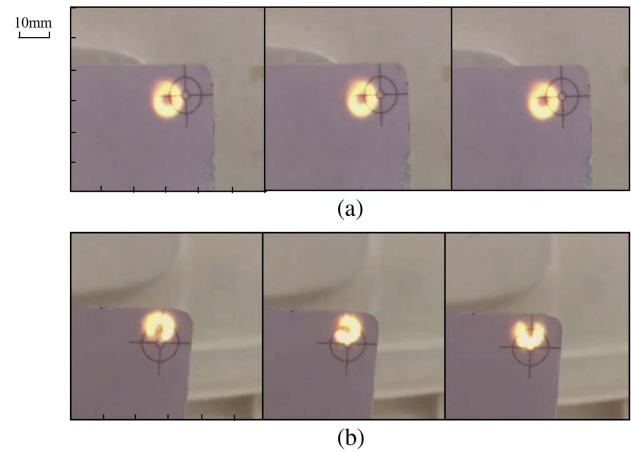


**Fig. 16.** Image of the scanning process with the same direction and constant velocity: (a) low speed, (b) high speed (see Visualization 1).

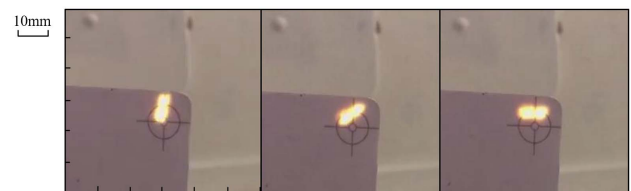


**Fig. 17.** Reverse isokinetic rotation scanning process image (see Visualization 2).

effectively corrected errors in the ideal scanned image with a symmetrical scan line around the origin. Finally, an experiment involving the dual-wedge fine-tuned mechanism under a reverse different rotation was carried out. The dual-wedge speed ratio was 8:-5, and low-speed scanning results are shown in Fig. 18. After superposition, the experimental images were mostly standard rose images because image acquisition was relatively fast, and a single image was only part of the image scanning; the scanned image was theoretically rose-shaped. With no angular error correction, the scanning path exhibited a petal shape with a significant cavity in the center. The experimental results showed no cavity in the center, indicating that the fine-tuning mechanism effectively corrected the angular error and ensured stability of the scanning image.

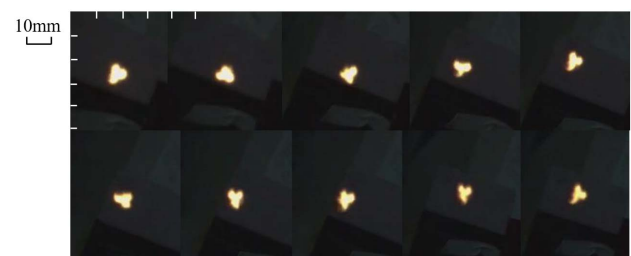


**Fig. 18.** Differential reverse scanning process image (see Visualization 3 and Visualization 4).

## 6. CONCLUSION

In this paper, a mathematical model of dual-wedge scanning and a physical model of optical trajectory are established, and the formula of the scanning trajectory under the effects of horizontal deviation and angular deviation is deduced. MATLAB simulation was used to conduct image scanning under various error conditions, which facilitated qualitative analysis. Results demonstrated that the angular error between the incident ray and the center axis of the optical wedge had the greatest influence on the scanning image. In dual-wedge reverse differential scanning, the deviation led to a significant increase in the number of petals, resulting in a large cavity in the center of the image. To eliminate angular deviation, a flexible cantilever beam, adjusting screw, and corresponding connector were designed to realize the two DOF elimination of the angular error. In this case, the angular error of the central optical axis was below 0.05 deg, ensuring accuracy of the scanning trajectory.

**Funding.** National Natural Science Foundation of China (NSFC) (51475305, 61473192).

## REFERENCES

1. J. Zhao, Y. Wu, L. Gao, H. Zhang, X. Yin, and Z. Yao, "Technology research on image motion compensation of the rotating double optical wedge," *Hongwai Yu Jiguang Gongcheng/Infrared Laser Eng.* **44**, 1506–1511 (2015).
2. Z. Fu, "Motion target recognition and tracking of infrared subpixel," *Signal Process.* **18**, 220–223 (2002).
3. J. Ge, Z. Chen, Y. D. Luo, J. Zhang, S. Zhan, H. H. Lin, J. J. Wang, and Q. H. Deng, "New double-wedge crystal depolarizer for monochromatic pulse light," *J. Appl. Opt.* **31**, 864–870 (2010).
4. Y. Yang, "Analytic solution of free space optical beam steering using Risley prisms," *J. Lightwave Technol.* **26**, 3576–3583 (2009).
5. A. Li, J. Sun, L. Wang, and L. Liu, "Submicroradian accuracy scanning system with a double-wedge rotating around the orthogonal axes," *Proc. SPIE* **5892**, 58921M (2005).
6. H. E. Lei, J. H. Yuan, L. I. Zhan, and J. R. Zhang, "Design of high-precision angle generator with double optical wedges," *OptoElectron. Eng.* **29**, 46–47 (2002).
7. Y. Li, "Closed form analytical inverse solutions for Risley-prism-based beam steering systems in different configurations," *Appl. Opt.* **50**, 4302–4309 (2011).
8. Y. Li, "Third-order theory of the Risley-prism-based beam steering system," *Appl. Opt.* **50**, 679–686 (2011).
9. Z. C. Wei, Y. W. Xiong, M. O. Wei, Q. F. Dai, and R. S. Liang, "Analysis for refractive property of rotary dual-wedge prism system and 2-d scanning trace," *J. Appl. Opt.* **30**, 939–943 (2009).
10. A. Li, W. Sun, W. Yi, and Q. Zuo, "Investigation of beam steering performances in rotation Risley-prism scanner," *Opt. Express* **24**, 12840–12850 (2016).
11. S. Xiao, Y. Li, X. Wu, and X. Bai, "Design of imaging guidance system with double optical wedges," in *Industrial Electronics and Applications* (2012), pp. 1473–1477.
12. A. Li, X. Gao, W. Sun, W. Yi, Y. Bian, H. Liu, and L. Liu, "Inverse solutions for a Risley prism scanner with iterative refinement by a forward solution," *Appl. Opt.* **54**, 9981–9989 (2015).
13. G. F. Marshall, *Handbook of Optical and Laser Scanning* (Marcel Dekker Inc., 2011).
14. G. F. Marshall, "Risley prism scan patterns," *Proc. SPIE* **3787**, 74–86 (1999).
15. V.-F. Duma and A. Schitea, "Laser scanners with rotational Risley prisms: exact scan patterns," *Proc. Rom. Acad. Ser. A* **19**, 53–60 (2018).
16. A. Li, Q. Zuo, W. Sun, and W. Yi, "Beam distortion of rotation double prisms with an arbitrary incident angle," *Appl. Opt.* **55**, 5164–5171 (2016).
17. S. W. Gong, "Perfectly flexible mechanism and integrated mechanism system design," *Mech. Mach. Theory* **39**, 1155–1174 (2004).
18. B. S. Shvartsman, "Direct method for analysis of flexible cantilever beam subjected to two follower forces," *Int. J. Non-Linear Mech.* **44**, 249–252 (2009).
19. C. A. DiMarzio and W. C. Warger, "Dual-wedge scanning confocal reflectance microscope," *Opt. Lett.* **32**, 2140–2142 (2007).
20. J. M. Gere and B. J. Goodno, *Mechanics of Materials* (Van Nostrand Reinhold Co., 1972).
21. J. J. Uicker and G. R. Pennock, *Theory of Machines and Mechanisms* (McGraw-Hill, 1980).